Scripta Materialia 207 (2022) 114277

Contents lists available at ScienceDirect

Scripta Materialia

journal homepage: www.elsevier.com/locate/scriptamat

Alloy design strategy for microstructural-tailored scandium-modified aluminium alloys for additive manufacturing

D. Schimbäck[a,b,*], P. Mair[c], M. Bärtl[a,d], F. Palm[a], G. Leichtfried[c], S. Mayer[b], P.J. Uggowitzer[e], S. Pogatscher[e]

[a] Airbus Central R & T, Airbus Defence and Space GmbH, Taufkirchen, Germany
[b] Department of Materials Science, Montanuniversität Leoben, Leoben, Austria
[c] Department of Mechatronics, Materials Science, Faculty of Engineering Sciences, University of Innsbruck, Innsbruck, Austria
[d] Institute of Materials Science, Universität der Bundeswehr München, Neubiberg, Germany
[e] Chair of Nonferrous Metallurgy, Montanuniversität Leoben, Leoben, Austria

ARTICLE INFO

Article history:
Received 13 July 2021
Revised 9 September 2021
Accepted 9 September 2021
Available online 24 September 2021

Keywords:
Aluminium alloys
Rapid solidification
Grain growth
Solidification microstructure
Laser powder bed fusion

ABSTRACT

To exploit the full potential of the additive layer manufacturing technique it is necessary to adapt the material to the process via a smart alloy design strategy. To this end, in order to derive and investigate various material concepts, the microstructural evolution of Sc-modified Al alloys was studied during the course of their production by laser powder bed fusion. Adding Mg as the main element (Al-4.4Mg-0.8Sc-0.3Zr-0.5Mn) generates an already-familiar bimodal microstructure. In contrast, if Cr is added as the main element (Al-2.6Cr-0.7Sc-0.3Zr), epitaxial grain growth takes place across several weld tracks, resulting in a distinct texture; and adding Ti as the main element (Al-1Ti-1Sc-0.4Zr) produces a uniform ultrafine-grained microstructure. The differences between these microstructures arise from interactions of the grain growth restriction factors and the solute with the primary precipitation structure. Thus, the precise manipulation of key metallurgical factors leads to novel materials which can be tailor-made for certain requirements.

Main Body

Additive manufacturing (AM), especially the laser powder bed fusion (LPBF) process of metallic materials, has attracted great interest in the materials science community over the last few decades. Characteristic of all powder-bed-based AM processes is the selective layer-by-layer melting or sintering of powder particles by an appropriate energy source, which makes complex structures, near-net shape geometries and the integration of multiple functional parts feasible [1,2]. Exceptional process conditions apply to this procedure, though: local overheating of the melt, high temperature gradients which generate rapid solidification and thermal stresses, segregation phenomena, non-equilibrium phases, anisotropy and textured materials [3–7]. Currently a variety of material classes adapted for conventional manufacturing techniques such as casting and forging are produced via LPBF [5,8–11]. Only a few of them, however, have been designed for the AM process in order to take full advantage of the processing conditions.

To design an Al alloy suitable for structural application in the aviation industry, balanced mechanical properties in terms of high strength values at a simultaneously high level of ductility are mandatory. Accordingly, the basic metallurgical mechanisms require accurate evaluation.

Alloying elements with high vapour pressure (Mg and Zn) tend to evaporate during the LPBF process [12]. This generates an unstable weld pool which favours the formation of spatter and increases the probability of material discontinuities [13]. Such alloying elements should therefore be avoided in powder-bed-based AM processes for processibility and performance reasons, and to allow the technology's deployment in future safety-relevant applications (e.g. aerospace).

With regard to microstructural evolution, many studies of AM materials have shown epitaxial grain growth in the material during the process, resulting in a textured material with anisotropic mechanical properties and (in the worst cases) pronounced segregations and hot cracking, [14–18]. Initial approaches to control the microstructure of various materials by adjusting the process parameters of AM processes have had only limited success [6,19–21]. To fully exploit the process-inherent characteristics, attractive design strategies also need to be implemented.

* Corresponding author.
E-mail address: david-erich.schimbaeck@airbus.com (D. Schimbäck).

https://doi.org/10.1016/j.scriptamat.2021.114277

Table 1
Metallurgical parameters for various binary alloys according to Easton et al. [24]

Element	Partitioning coefficient k	Slope of the liquidus line m [K/wt.%]	$m(k-1)$	Maximum concentration [wt.%]
Si	0.11	-6.6	5.9	≈12.6
Cu	0.14	-3.4	2.8	33.2
Mg	0.51	-6.2	3.0	≈3.4
Zr	2.5	4.5	6.8	0.11
Cr	2.0	3.5	3.5	≈0.4
Ti	9.0	30.7	245.6	0.15

A generally accepted instrument for effective estimation of grain refinement even during solidification is the grain growth restriction factor Q (GRF) [22,23]. It should be noted that in LPBF grain refinement can be established only during solidification, as a subsequent forming and recrystallization step is not practicable in this near-net shape process. The GRF describes the segregation tendency ahead of the solidification front and can be directly derived from the phase diagram for binary systems as follows:

$$GRF = m(k-1)C_0 \quad (1)$$

where m is the slope of the liquidus line in the binary phase diagram, k the equilibrium partition coefficient and C_0 the composition of the binary alloy. Table 1 gives a comparison of alloying elements usually used in Al alloys and their metallurgical parameters k and m in their binary system with Al. It is obvious that Ti, in particular, has comparably high values, which according to the GRF makes it an attractive option for grain refinement.

It is obvious that Ti, in particular, has comparably high values of $m(k-1)$, which makes it an attractive option for grain refinement. Nevertheless, due to its limited solubility (see Table 1) Ti is mostly added in a comparable low concentration, but not as main alloying element. Commonly it is considered as an inoculant grain refiner in the form of TiB_2 or as TiC. Here extensive studies of the underlying mechanisms during conventional processing routes have already been published [25–28]. Only a few authors have investigated Ti as a main alloying element with its effect via grain growth restriction, mostly addressing solidification rates in conventional processing [29–34]. Recently, preliminary studies have been published where Ti was added to the conventional Al alloy 2024 processed by LPBF with the aim of significantly decreasing grain size and thus of suppressing hot cracking [35–37]. Adding Ti to conventional Al alloys thus appears as a promising approach in improving the LPBF processibility.

Due to the high cooling rates of the LPBF process, most of the alloying elements are supersaturated in the as-built state, enabling economically advantageous heat treatments without additional solution annealing steps [38,39]. Studies on the Scalmalloy® and Scancromal® concepts proved Sc and/or Zr to be best suited for LPBF process conditions [3,40–42]. Even the addition of small amounts promotes the formation of nano-sized, $L1_2$-structured, (semi-)coherent Al_3Sc or $Al_3(Sc_xZr_{1-x})$ precipitates [43–47]. These act both as solidification nuclei and, after a precisely adjusted heat treatment, as a hardening phase and facilitate a significant increase in strength [48].

Adding Sc and Ti to an Al alloy with various high Mg contents was already investigated by Wang et al. [49] to assess its very favourable influence on the grain size of the microstructure and mechanical properties, but only in a diluted concentration of 0.2 wt.% Sc and 0.15 wt.% Ti.

The aim of this work is to design a process-robust and high-strength Sc-modified Al-Ti alloy (Scantital®) on the basis of the 1st-generation Scalmalloy® [50] and 2nd-generation Scancromal® [51] of Airbus, utilizing basic metallurgical concepts. In contrast to the previous studies on Ti addition to conventional Al alloys to enhance processibility [36,37], it aims to create a new alloy tailored to the LPBF process and adapted for high strength applications by precipitation hardening of Sc and Zr.

Table 2
Chemical composition in wt.% of all Sc-modified Al alloys Scalmalloy®, Scancromal® and Scantital® investigated, and the respective values for GRF, determined via the initial rate of constitutional supercooling [54].

Alloy	*Al*	*Mg*	*Cr*	*Ti*	*Sc*	*Zr*	Mn	*GRF [K]*
Al-Sc-Zr *Base alloy*	Bal.	-	-	-	1.0	0.4	-	0.01
Al-Mg-Sc-Zr-Mn *Scalmalloy®*	Bal.	4.4	-	-	0.8	0.3	0.5	16.3
Al-Cr-Sc-Zr *Scancromal®*	Bal.	-	2.6	-	0.7	0.3	-	2.0
Al-Ti-Sc-Zr *Scantital®*	Bal.	-	-	1.0	1.0	0.4	-	18.4

The powder chemistry of the various alloys investigated in this work is shown in Table 2. The powder of the Al-Sc-Zr base alloy was produced via melt spinning and extrusion, and atomized by ECKART TLS GmbH, Germany via electrode induction melting inert gas atomization (EIGA), and the Scalmalloy® and Scancromal® alloy powders were produced via inert gas atomization (IGA) by Toyo Aluminium K.K, Japan. To achieve the chemical composition of Scantital®, the Al-Sc-Zr base powder was mechanically alloyed with nano-Ti-powder by Nanografi Nanotechnology AS, Germany.

The LPBF process was conducted using an SLM®125 machine at Airbus Central R & T in Munich, Germany and an AconityLab® machine at the Department of Mechatronics at the University of Innsbruck, Austria. A parameter study using cubic specimens of 10 × 10 × 10 mm³ was performed to obtain fully dense specimens. All alloys were investigated in metallographic cross-section by scanning electron microscopy (SEM) Zeiss Auriga 40 equipped with an Oxford Nordlysnano electron back-scattered diffraction (EBSD) detector in back-scattered electron (BSE) mode and by EBSD. The EBSD measurements were evaluated using MTEX Toolbox 5.6.1 on Matlab R2017b. For an outlook regarding mechanical properties, hardness measurements according to DIN EN ISO 6506 (HBW2.5/62.5) were conducted on the parameter cubes using an Instron Wolpert GmbH Digi-Testor 930 [52]. The isopleth diagrams were created using the Pandat™ software package for multi- component systems, with input from the PanAl2019 [53] database. The GRFs of the multicomponent systems (Table 2) were calculated according to procedure described by Schmid-Fetzer and Kozlov [54], taking into account the initial rate of constitutional supercooling.

The microstructures of the various alloys are shown in Figs. 1 and 2. Compared to the base alloy (Fig. 1a), which only contains the grain-refining elements Sc and Zr, it is apparent that changing the main alloying element from Mg (Fig. 1b) to Cr (Fig. 1c) and Ti (Fig. 1d) has a significant influence on the solidification microstructure. In the base alloy (Figs. 1a and 2a) a bimodal microstructure is observed, with irregularly shaped fine-grained areas that do not define the weld pool geometry as clearly as in Scalmalloy®. A low hardness value of 52 HBW2.5/62.5 was also measured for the base Al-1Sc-0.4Zr alloy. This can be traced back to the as-built state and the lack of solid solution hardening elements.

Adding Mg to the base alloys produces a microstructure with clearly delineated fine-grained areas with grain sizes of 500 – 700nm and coarse-grained areas with columnar grains of 1 – 10µm in size (Figs. 1b and 2b), which is in accordance with literature [3,40,41,48,50,55–58]. Within the coarse-grained areas, a <100>-texture reveals solidification along the highest thermal gradient towards the top of the weld pool. The overall hardness of 116 HBW2.5/62.5 is attributed to both the partial ultrafine-grained (UFG) microstructure and solid solution hardening by Mg. Mg is considered a very effective solid solution hardening element that

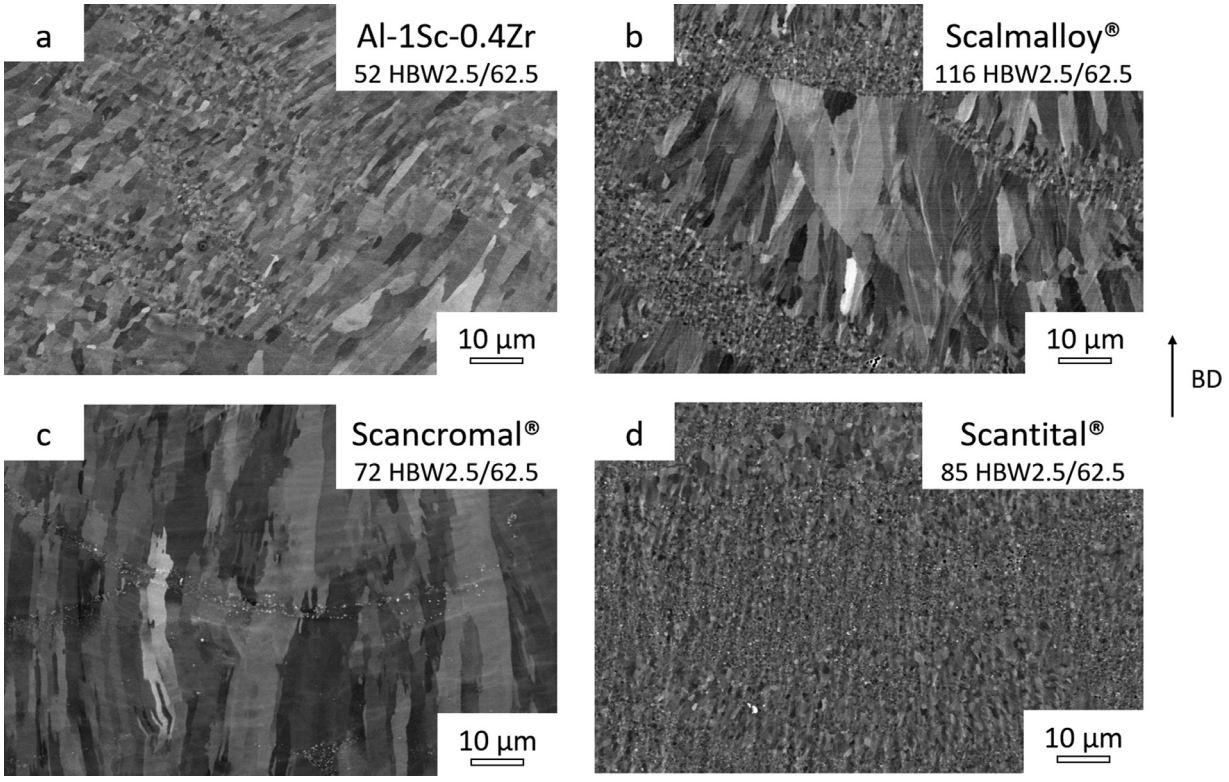

Fig. 1. SEM images taken in BSE mode of all alloys investigated in the as-built state with their respective hardness values: a) Al-1Sc-0.4Zr base alloy with a bimodal microstructure; b) Scalmalloy® with its typical bimodal microstructure; c) Scancromal® with clearly visible epitaxial grain growth across the different weld tracks; d) Scantital® with ultrafine-grained equiaxed microstructure. The right-hand arrow indicates the build direction (BD).

also significantly increases the Hall-Petch coefficient, which in turn exploits the potential of the UFG microstructure [59,60]. Unfortunately, however, Mg shows a high vapor pressure, which reduces the reliability of the LPBF process due to the difficult-to-control interaction of the laser beam with the metal vapor [61].

Modification with Cr in Scancromal® causes clearly epitaxial grain growth across various weld tracks (Figs. 1c and 2c); this was already reported by Palm et al. [51].The layers themselves are indicated clearly by a seam of precipitates, probably $Al_{11}Cr_2$ or $Al_{13}Cr_2$/ Al_7Cr, as seen in Fig. 1. The EBSD image in Fig. 1c also shows a distinct, preferred growth orientation, which results in a strongly pronounced <100>-texture in the fcc Al matrix along the build direction (BD). Due to this coarse microstructure the average hardness of Scancromal®, 71 HBW2.5/62.5, is comparatively low.

In contrast to Scancromal®, and as expected from the high value of the GRF, the microstructure of Scantital® shows a UFG equiaxed microstructure with no preferred solidification orientation with an average grain size of approximately 500 nm (Figs. 1d and 2d). Because of the monomodal UFG structure, the hardness value yields 85 HBW2.5/62.5. Compared to Scalmalloy®, the lack of approximately 30 hardness points may stem from missing solid solution hardening of Mg and Mn [62].

A basic understanding of the grain formation mechanism during solidification was already detailed by Easton and StJohn in the context of the Interdependence Theory [24,63–65]. This theory describes the influence of the segregation tendency of the main alloying elements in the remaining melt during solidification, which generates more or less pronounced constitutional supercooling (CS) depending on the GRF and the initial concentration. In [64], the distance between two nucleation events x_{gs}, which basically determines the grain size d_{gs}, can be divided into three different parts: x_{cs}, the distance a grain has to grow to establish sufficient CS; x'_{dl}; the distance from the solid-liquid (S/L) interface to the position where sufficient CS is established to activate a potent nuclei; and x_{sd}, the distance from where sufficient CS is established up to the next most potent nuclei in the melt:

$$x_{gs} = x_{cs} + x'_{dl} + x_{sd} \tag{2}$$

For a full mathematical description of the various terms, see [24,63–65]. Recently this concept was also studied by various authors with respect to the special process conditions of AM [66–68]. At higher cooling rates and higher thermal gradients thermal supercooling becomes more important, but the basic principles of alloy-specific constitutional supercooling remain unaffected.

We will now consider the nucleation and supercooling conditions for the different alloy variants. Starting with the base alloy, the melt itself is inoculated with highly potent primary $Al_3(Sc_xZr_{1-x})$ precipitates, which act as nucleation sites for the α-Al [3]. A very similar situation is demonstrated by Scalmalloy®. Comparing the microstructures of the base alloy and Scalmalloy®, it becomes apparent that fewer nuclei have been activated in the base alloy. Thus it can be assumed that thermal undercooling alone is not sufficient to activate a major portion of these nucleation sites, causing a minor volume fraction of fine-grained areas (also irregularly shaped) to form. On the contrary, by adding 4.4 wt.% Mg according to the Scalmalloy® concept, a GRF of 16.3 K can be assessed (Table 2). This additional contribution of supercooling seems to be sufficient to activate a major portion of primary $Al_3(Sc_xZr_{1-x})$ precipitates, producing a regular bimodal microstructure. Whether this additional contribution by the solute stems from the GRF (constitutional) or from the influence of the surface energy and the S/L growth rate (thermal) needs further investigations.

The multicomponent system Scancromal® with Cr as the main alloying element exhibits a GRF of only 2.0. Thus, in terms of constitutional supercooling, Scancromal® is comparable to the base

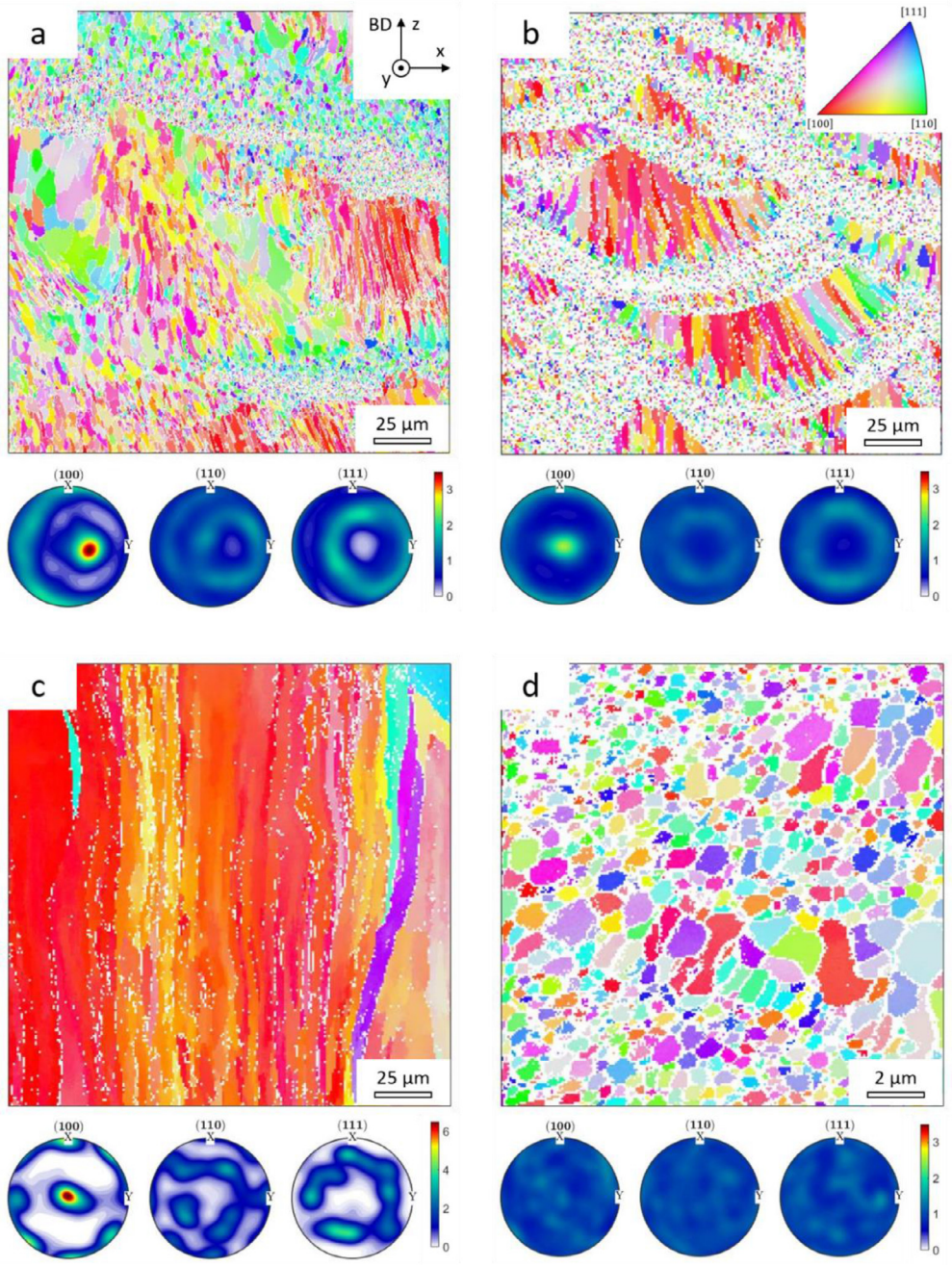

Fig. 2. Results of the overview EBSD mappings (200 × 200 µm² for a, b, c and 15 × 15 µm² for d) showing the inverse pole figure maps in z direction (IPFz) aligned parallel to the build direction (BD)(white areas are not indicated regions) and the calculated (100), (110) and (111) pole figures (PF), respectively: a) Al-1Sc-0.4Zr base alloy, with irregular-shaped bimodal microstructure and a weak pronounced favoured <100> growth direction along the build direction; b) Scalmalloy®, with its typical regular bimodal microstructure and a distinct <100>-texture along the build direction due to the coarse grained area; c) Scancromal®, showing clearly epitaxial grain growth across the weld tracks and a strongly pronounced <100> texture along the build direction (note the adapted scale of the PF); and d) Scantital, showing a randomly oriented ultrafine-grained microstructure with no noticeable texture (note the different magnification for the mapping). All alloys were investigated in the as-built state.

alloy. In contrast to the base alloy, however, primary $Al_{11}Cr_2$ or $Al_{13}Cr_2$/ Al_7Cr are formed in the Cr variant (Figs. 3 and 4). Both the $Al_{11}Cr_2$ phase and the Al_7Cr phase exhibit a monoclinic crystal structure [69–72], with significant mismatch to the fcc Al-matrix. Consequently they also do not act as potent nuclei. Rather, initial studies indicate that Sc and Zr are incorporated into the Cr phases, and thus the number density of the $Al_3(Sc_xZr_{1-x})$ precipitates decreases (note: Details of this cannibalisation effect will be published in a future work). The lack of suitable nuclei and the low GRF consequently generate a microstructure characterised by epitaxial grain growth.

Adding Ti as the main alloying element, on the other hand, results in a GRF value of 18.4 K. Because the GRF of Scantital® is comparable to that of Scalmalloy®, one would assume a similar microstructure. However, next to the CS, Ti leads to the formation of Al_3Ti precipitates (Figs. 3 and 4). This phase is known to form in a high-temperature cubic type $L1_2$ structure and in low-temperature tetragonal type DO_{22}, although it has not been definitively clarified as to which type predominates in rapid solidification at LPBF [73–75]. Based on the UFG microstructure, it can be assumed that in our case potent $L1_2$ Al_3Ti precipitates were formed. It is also known that Ti can replace Sc in Al_3Sc while

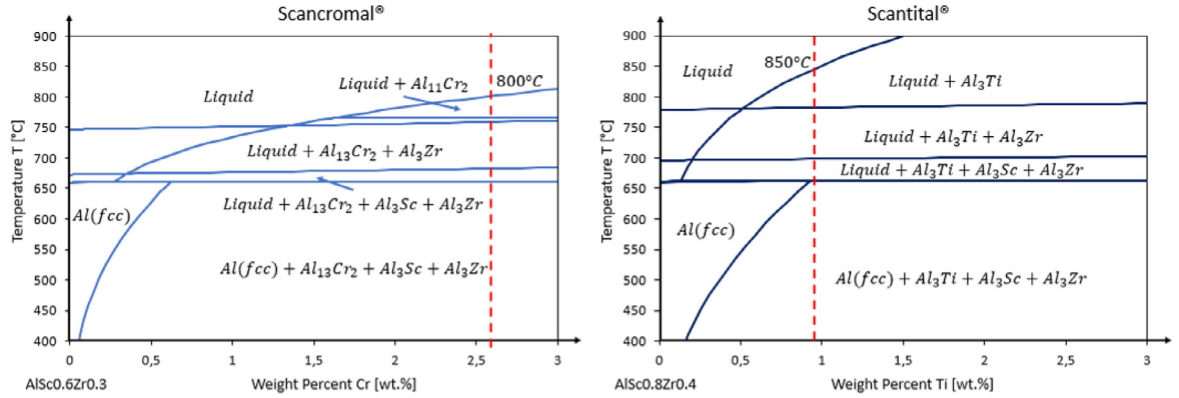

Fig. 3. Isopleths of Scancromal and Scantital; phase compositions of Scancromal® and Scantital® are indicated with the red dashed line and their liquidus temperature.

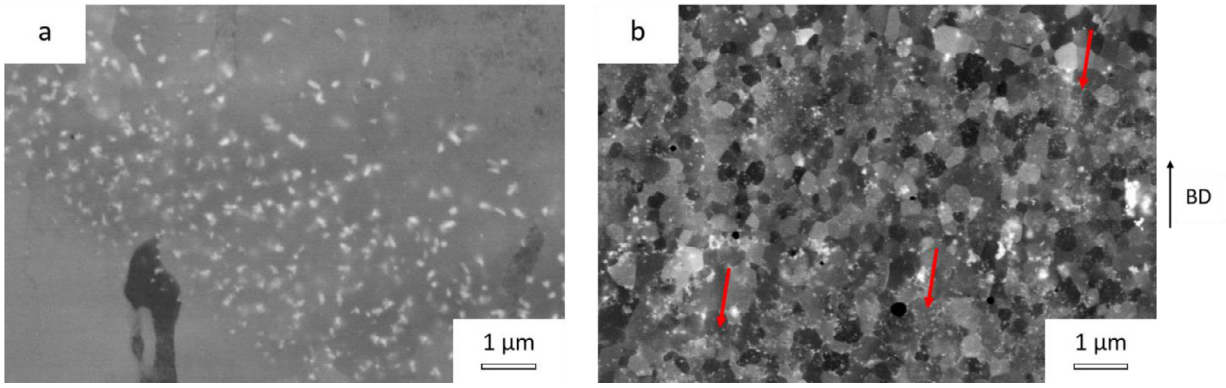

Fig. 4. Higher magnification SEM images taken in BSE mode of a) Scancromal®, with comparable coarse Al-Cr precipitates and b) Scantital®, with finely dispersed Al-Ti precipitates indicated by red arrows. The right-hand arrow indicates the build direction (BD).

retaining the $L1_2$ structure [76,77], which suggests an increased number density of $Al_3(Sc, Zr, Ti)$. Thus, both Al_3Ti and $Al_3(Sc, Zr, Ti)$ presumably contribute to a decrease in the x_{sd} value in Eq. (2). Hence, Ti contributes to grain refinement through both a high GRF value and the precipitates inherent in its alloy system.

In summary, adding various main alloying elements (Mg, Cr and Ti) to the base alloy Al-1Sc-0.4 Zr has a major impact on microstructural evolution during the rapid solidification of the LPBF process. If Mg is added in a hypo-eutectic concentration of 4.4 wt.% a bimodal microstructure is obtained; whereas adding Cr and Ti in a hyper-peritectic concentration generates epitaxial grain growth across various weld tracks, with a pronounced texture in the case of Cr, and a very desirable UFG microstructure in case of Ti. Constitutional supercooling and thus GRF, and the introduction of potent heterogeneous nucleation sites, both prove to be helpful adjustment tools for adapting the microstructure of Al alloys to specific applications.

Declaration of Competing Interest

The authors declare the following financial interests/personal relationships which may be considered as potential competing interests.

References

[1] Additive Manufacturing - Design - Part 1, Laser-Based Powder Bed Fusion of Metals, 2020.
[2] A. Gebhardt, in: Carl Hanser Verlag GmbH & Co. KG, München, 2016.
[3] A.B. Spierings, K. Dawson, T. Heeling, P.J. Uggowitzer, R. Schäublin, F. Palm, K. Wegener, Mater. Des. 115 (2017) 52–63.
[4] K. Kempen, L. Thijs, J. Van Humbeeck, J.-P. Kruth, Phys. Procedia 39 (2012) 439–446.
[5] L. Thijs, F. Verhaeghe, T. Craeghs, J. Van Humbeeck, J.-P. Kruth, Acta Mater 58 (2010) 3303–3312.
[6] R. Shi, S.A. Khairallah, T.T. Roehling, T.W. Heo, J.T. McKeown, M.J. Matthews, Acta Mater 184 (2020) 284–305.
[7] P.A. Hooper, Addit. Manuf. 22 (2018) 548–559.
[8] A. Khorasani, I. Gibson, U.S. Awan, A. Ghaderi, Addit. Manuf. 25 (2019) 176–186.
[9] A. Maamoun, Y. Xue, M. Elbestawi, S. Veldhuis, Materials (Basel) 12 (2018) 12.
[10] N. Read, W. Wang, K. Essa, M.M. Attallah, Mater. Des. 65 (2015) 417–424.
[11] D. Gu, Laser Additive Manufacturing of High-Performance Materials, Springer Berlin Heidelberg, Berlin, Heidelberg, 2015.
[12] F. Ahsan, L. Ladani, JOM 72 (2020) 429–439.
[13] J.P. Oliveira, T.G. Santos, R.M. Miranda, Prog. Mater. Sci. 107 (2020) 100590.
[14] A. Basak, S. Das, Annu. Rev. Mater. Res. 46 (2016) 125–149.
[15] J.P. Oliveira, A.D. LaLonde, J. Ma, Mater. Des. 193 (2020) 108762.
[16] X. Wu, J. Liang, J. Mei, C. Mitchell, P.S. Goodwin, W. Voice, Mater. Des. 25 (2004) 137–144.
[17] M. Ma, Z. Wang, X. Zeng, Mater. Sci. Eng. A 685 (2017) 265–273.
[18] W. Stopyra, K. Gruber, I. Smolina, T. Kurzynowski, B. Kuźnicka, Addit. Manuf. 35 (2020) 101270.
[19] G.P. Dinda, A.K. Dasgupta, J. Mazumder, Scr. Mater. 67 (2012) 503–506.
[20] P. Liu, Z. Wang, Y. Xiao, M.F. Horstemeyer, X. Cui, L. Chen, Addit. Manuf. 26 (2019) 22–29.
[21] H. Choo, K.-L. Sham, J. Bohling, A. Ngo, X. Xiao, Y. Ren, P.J. Depond, M.J. Matthews, E. Garlea, Mater. Des. 164 (2019) 107534.
[22] D.H. StJohn, M. Qian, M.A. Easton, P. Cao, Z. Hildebrand, Metall. Mater. Trans. A 36 (2005) 1669–1679.
[23] A. Greer, A. Bunn, A. Tronche, P. Evans, D. Bristow, Acta Mater 48 (2000) 2823–2835.
[24] M.A. Easton, D.H. StJohn, Metall. Mater. Trans. A 30 (1999) 1613–1623.
[25] P. Schumacher, A.L. Greer, J. Worth, P.V. Evans, M.A. Kearns, P. Fisher, A.H. Green, Mater. Sci. Technol. 14 (1998) 394–404.
[26] B.S. Murty, S.A. Kori, M. Chakraborty, Int. Mater. Rev. 47 (2002) 3–29.
[27] K.T. Kashyap, T. Chandrashekar, Bull. Mater. Sci. 24 (2001) 345–353.
[28] Y. Wang, Z. Zhang, W. Wang, X. Bian, Mater. Sci. Eng. A 366 (2004) 17–24.
[29] J. Cissé, H.W. Kerr, G.F. Bolling, Metall. Trans. 5 (1974) 633–641.
[30] D.H. StJohn, L.M. Hogan, J. Mater. Sci. 15 (1980) 2369–2375.
[31] K. Venkateswarlu, S.. Das, M. Chakraborty, B.. Murty, Mater. Sci. Eng. A 351 (2003) 237–243.
[32] J.F. Nie, A. Majumdar, B.C. Muddle, Mater. Sci. Eng. A (1994) 619–624 179–180.
[33] J.F. Nie, S. Sridhara, B..C. Muddle, Metall. Trans. A 23 (1992) 3193–3205.
[34] S.S. Nayak, S.K. Pabi, D.H. Kim, B.S. Murty, Intermetallics 18 (2010) 487–492.
[35] P. Mair, L. Kaserer, J. Braun, N. Weinberger, I. Letofsky-Papst, G. Leichtfried, Mater. Sci. Eng. A 799 (2021) 140209.

[36] Q. Tan, J. Zhang, Q. Sun, Z. Fan, G. Li, Y. Yin, Y. Liu, M.-X. Zhang, Acta Mater 196 (2020) 1–16.
[37] J. Zhang, J. Gao, B. Song, L. Zhang, H. Changjun, C. Cai, K. Zhou, Y. Shi, Addit. Manuf. (2020) 101829.
[38] D. Knoop, A. Lutz, B. Mais, A. von Hehl, Metals (Basel) 10 (2020) 514.
[39] T. Maeshima, K. Oh-ishi, Heliyon 5 (2019).
[40] A.B. Spierings, K. Dawson, K. Kern, F. Palm, K. Wegener, Mater. Sci. Eng. A 701 (2017) 264–273.
[41] A.B. Spierings, K. Dawson, P.J. Uggowitzer, K. Wegener, Mater. Des. 140 (2018) 134–143.
[42] H. Zhang, D. Gu, J. Yang, D. Dai, T. Zhao, C. Hong, A. Gasser, R. Poprawe, Addit. Manuf. 23 (2018) 1–12.
[43] E.A. Marquis, D.N. Seidman, Acta Mater 49 (2001) 1909–1919.
[44] K.B. Hyde, A.F. Norman, P.B. Prangnell, Acta Mater 49 (2001) 1327–1337.
[45] W. Lefebvre, N. Masquelier, J. Houard, R. Patte, H. Zapolsky, Scr. Mater. 70 (2014) 43–46.
[46] F. Jiang, J. Zhou, H. Huang, J. Qu, Mater. Res. Innov. 18 (2014) S4–228 S4-234.
[47] V.V. Zakharov, Met. Sci. Heat Treat. 56 (2014) 281–286.
[48] D. Schimbäck, M. Panzenböck, F. Palm, Pract. Metallogr. 56 (2019) 797–812.
[49] X. Wang, G. Chen, B. Li, L. Wu, D. Jiang, Rare Met 29 (2010) 66–71.
[50] K. Schmidtke, F. Palm, A. Hawkins, C. Emmelmann, Phys. Procedia 12 (2011) 369–374.
[51] F. Palm, M. Bärtl, D. Schimbäck, A. Maier, in: 11th CIRP Conf. Photonic Technol. [LANE 2020], 2020.
[52] DIN EN ISO 6506-1: Metallic Materials – Brinell Hardness Test – Part 1: Test Method (ISO 6506-1:2014), 2014.
[53] CompuTherm-LCC, 2019.
[54] R. Schmid-Fetzer, A. Kozlov, Acta Mater 59 (2011) 6133–6144.
[55] J.P. Best, X. Maeder, J. Michler, A.B. Spierings, Adv. Eng. Mater. 21 (2019) 1801113.
[56] A.B. Spierings, K. Dawson, P. Dumitraschkewitz, S. Pogatscher, K. Wegener, Addit. Manuf. 20 (2018) 173–181.
[57] A.B. Spierings, K. Dawson, M. Voegtlin, F. Palm, P.J. Uggowitzer, CIRP Ann. 65 (2016) 213–216.
[58] K. Schmidtke, F. Palm, in: 9th Int. Conf. Trends Weld, Res. Am. Soc. Met. (2012).
[59] P. Ebenberger, P.J. Uggowitzer, B. Gerold, S. Pogatscher, Materials (Basel) 12 (2019).
[60] P. Ebenberger, P.J. Uggowitzer, S. Kirnstötter, B. Gerold, S. Zaefferer, S. Pogatscher, Scr. Mater. 166 (2019) 64–67.
[61] A. Ladewig, G. Schlick, M. Fisser, V. Schulze, U. Glatzel, Addit. Manuf. 10 (2016) 1–9.
[62] Ø. Ryen, B. Holmedal, O. Nijs, E. Nes, E. Sjölander, H.-E. Ekström, Metall. Mater. Trans. A 37 (2006) 1999–2006.
[63] M.A. Easton, D.H. StJohn, Metall. Mater. Trans. A 30 (1999) 1625–1633.
[64] D.H. StJohn, M. Qian, M.A. Easton, P. Cao, Acta Mater 59 (2011) 4907–4921.
[65] M.A. Easton, D.H. StJohn, Acta Mater 49 (2001) 1867–1878.
[66] D. Zhang, A. Prasad, M.J. Bermingham, C.J. Todaro, M.J. Benoit, M.N. Patel, D. Qiu, D.H. StJohn, M. Qian, M.A. Easton, Metall. Mater. Trans. A 51 (2020) 4341–4359.
[67] A. Prasad, L. Yuan, P. Lee, M. Patel, D. Qiu, M. Easton, D. StJohn, Acta Mater 195 (2020) 392–403.
[68] M. Bermingham, D. StJohn, M. Easton, L. Yuan, M. Dargusch, JOM 72 (2020) 1065–1073.
[69] M.J. Cooper, Acta Crystallogr 13 (1960) 257–263.
[70] Y. Liang, C. Guo, C. Li, Z. Du, J. Alloys Compd. 460 (2008) 314–319.
[71] B.B. Cao, K.H. Kuo, J. Alloys Compd. 458 (2008) 238–247.
[72] J.L. Murray, J. Phase Equilibria 19 (1998) 367–375.
[73] Y.V. Milman, D.B. Miracle, S.I. Chugunova, I.V. Voskoboinik, N.P. Korzhova, T.N. Legkaya, Y.N. Podrezov, Intermetallics 9 (2001) 839–845.
[74] M.B. Winnicka, R.A. Varin, Scr. Metall. Mater. 25 (1991) 2297–2302.
[75] T. Hanamura, T. Sugai, M. Tanino, J. Mater. Sci. 25 (1990) 3286–3290.
[76] Y. Harada, D.C. Dunand, Mater. Sci. Eng. A (2002) 686–695 329–331.
[77] M.E. van Dalen, D.C. Dunand, D.N. Seidman, Acta Mater 53 (2005) 4225–4235.